Check for updates

Sequential treatment of cyanide and phenolic mixtures using CMC-PVP-nZVI/Pd and *Rhodococcus pyridinivorans* strain PDB9T N1

Ankita Priyadarshini,[a] Naresh Kumar Sahoo, [ID] *[a] Soumya Mishra,[a]
Prasant Kumar Sahoo,[b] Ranjan Kumar Bhuyan,[c] Prangya Ranjan Rout[d]
and Bankim Chandra Tripathy[e]

Cyanide and phenol are considered the major toxic pollutants in coke-oven wastewater. Cyanide, at a pH less than 10, is converted to HCN gas ($pK_a = 9.2$). Hence, cyanide treatment requires strongly alkaline conditions, *i.e.*, a pH of more than 10; however, at such a high pH, the viability of microbes is not feasible. Therefore, to overcome this incompatibility, a sequential nano-bio treatment system was developed, integrating a novel carboxymethyl cellulose-polyvinylpyrrolidone-stabilized nanoscale zero-valent iron doped with palladium (CMC-PVP-nZVI/Pd) nanocomposite, followed by bio-treatment using *R. pyridinivorans* strain PDB9T N-1. The first nanostage was operated at pH 12 to stabilize cyanide (CN^-) and initiate its removal, while the subsequent biostage was operated at a pH of 7.4 to achieve the complete removal of phenol. To prevent the atmospheric oxidation of nZVI and to improve its reusability and electron mobility, it was doped with palladium and conjugated with CMC and PVP. The synthesised nanomaterials were characterized using XRD, FTIR spectroscopy, FESEM, EDX, and XPS analyses. Results revealed that about 99% of cyanide was removed with an initial dose of 100 mg L^{-1} at 30 °C using the nanocomposite, followed by the complete biodegradation of the remaining phenol (300 mg L^{-1}). The cyanide removal efficiency of the nanocomposite was 1.8-fold higher than that of the bare nZVI. Overall, the cyanide removal process followed a pseudo-2nd-order kinetics model, revealing a chemisorption nature with a superior sorption capacity of 93.37 mg g^{-1}. The intraparticle diffusion model showed that exterior mass transfer primarily governed the cyanide removal. Additionally, the nanocomposite exhibited strong reusability, demonstrating the efficacy of the proposed sequential nano-bio system.

1. Introduction

Steel plant industries generate vast amounts of wastewater primarily from coke oven plants, varying in the range of 0.3 to 4 m³ per ton of coke production.[1,2] In general, coke-oven wastewater contains high levels of phenol (ranging from 150 to 2000 mg L^{-1}) and cyanide (ranging from 0.1 to 0.6 kilograms per ton of coke), significantly surpassing the standard limits for phenol at 1 mg L^{-1} and cyanide at 0.2 mg L^{-1}.[3,4] Cyanide inhibits the cytochrome oxidase enzyme system and,

subsequently, the mitochondrial electron transport chain and adenosine triphosphate (ATP) formation, thus causing serious human health hazards.[5,6] Similarly, phenolic compounds cause significant human health and environmental damages due to their acute toxicity and carcinogenic nature.[7,8] Thus, cyanide and phenolic compounds are listed as priority pollutants by the United States Environmental Protection Agency (USEPA).[6,9]

Conventional treatment methods such as chlorination, photocatalysis, electrolysis, and membrane filtration are often not cost-effective and typically result in only the partial degradation of pollutants, leading to the formation of harmful secondary intermediates. Among biological treatment methods, reactors based on the activated sludge process are most frequently utilized for this wastewater.[7,10] In general, several studies have reported cyanide biodegradation, with most experiments conducted at neutral or sub-alkaline pH (<10). However, at pH values below 10, cyanide (CN^-) is converted to hydrogen cyanide (HCN) gas,[11] and the authors of these studies often did not verify whether cyanide removal occurred through microbial degradation or volatilization as HCN.[11,12] Therefore, industrial wastewater containing cyanide must be maintained

[a]Department of Chemistry, Environmental Science and Technology Program, Faculty of Engineering and Technology (ITER), Siksha 'O' Anusandhan (Deemed to be University), Bhubaneswar 751030, Odisha, India. E-mail: nareshsahoo@soa.ac.in; nareshks2010@gmail.com

[b]Environmental Hydrology Division, National Institute of Hydrology, Jalvigyan Bhawan, Roorkee 247667, India

[c]P. G. Department of Physics, Government Autonomous College Angul Odisha, India

[d]Department of BioTechnology, Dr B. R Ambedkar National Institute of Technology Jalandhar, India

[e]Faculty of Chemical Sciences (AcSIR), Department of Hydro and Electrometallurgy, Institute of Minerals and Materials Technology, Bhubaneswar 751 013, India

at an alkaline pH above 10 ($pK_a = 9.2$) to prevent HCN gas formation.[13] Nonetheless, at pH levels higher than 10, microbial viability and effective cyanide biodegradation are limited.[14] To address these challenges, the present study adopted a two-stage sequential nano-bio treatment strategy. In the first stage, a nanocomposite was applied under alkaline conditions for rapid cyanide removal. This was followed by pH adjustment and aeration, after which a bacterial strain was grown at a pH of 7.4 to completely degrade phenol and remaining intermediates. Such combined approaches are now increasingly recognized for their ability to merge redox catalysis and biological oxidation, resulting a safer and more comprehensive remediation.[15]

Nanoscale zero-valent iron (nZVI) has emerged as a promising candidate for on-site remediation of toxic heavy metals,[16] halogenated hydrocarbons,[17,18] and other pollutants.[19] Its appeal lies in its nontoxicity, high reactivity, rapid kinetics, and large specific surface area, which collectively enable efficient contaminant removal from water.[20–23] However, several challenges limit its effectiveness. In particular, nZVI particles readily agglomerate due to their nanoscale size and intrinsic magnetic properties,[24,25] leading to a transition from the nanoscale to the microscale. This agglomeration diminishes their specific surface area, mobility, and overall reactivity.[26,27] Secondly, nZVI is highly reactive and can readily interact with water and oxygen, which reduces its long-term effectiveness. To address these challenges, several strategies have been developed. A common approach to prevent particle aggregation involves using ecofriendly biopolymers such as chitosan and carboxymethyl cellulose (CMC). CMC, in particular, is a nontoxic, biodegradable polymer that forms a protective coating around nZVI particles. This coating generates electrostatic and steric repulsion forces, which keep the particles apart, thereby enhancing their stability and dispersion in water.[28,29] The CMC stabilization process enables nZVI to remain suspended for longer durations, thereby increasing its contact time with environmental contaminants and enhancing remediation efficiency. Similarly, polyvinylpyrrolidone (PVP), a conductive polymer, has attracted attention as a modifying agent because of its distinct properties, including low scattering loss and sufficient charge storage capacity. The pyrrole group of PVP allows it to interact with other molecules, form complexes with salts, and act as a stabilizer, which improves particle dispersion and may also contribute to redox reactions involving nZVI. Consequently, PVP was employed in this study to enhance both the efficiency and stability of nZVI. However, due to the high reactivity of nZVI, oxidation readily occurs upon exposure to air or water, producing a core–shell structure with metallic iron at the core and iron oxides on the surface. CMC and PVP together facilitate a well-stabilized hybrid network that enhances nanoscale reactivity and extends the catalyst lifetime.[30] Another strategy for enhancing nZVI's performance is the deposition of secondary metals such as Pd, Pt, or Ni onto its surface. Recent advances indicate that modified or doped nZVI systems exhibit superior degradation efficiency *via* the synergistic activation of oxidants and electron transfer.[31,32] This modification increases the availability of electrons for contaminant reduction, thereby improving nZVI's reactivity. Among

these, Pd has been widely recognized as the most effective catalyst due to its excellent chemical stability and superior catalytic activity.[33] When Pd^{4+} ions are introduced, they impede the oxidation of iron particles by accepting electrons to reduce to Pd^{2+}, thereby protecting nZVI from oxidation and facilitating the formation of Fe–Pd bimetallic nanoparticles.[34] According to recent reports, oxygen-promoted redox pathways and partial denitrification systems can further increase the effectiveness of oxidative transformation.[35,36] In certain cases, this modification also improves nanoparticle stability under aerobic conditions by further inhibiting surface oxidation.[23]

Based on these principles, a carboxymethyl cellulose-polyvinylpyrrolidone-stabilized nanoscale zero-valent iron/palladium (CMC-PVP-nZVI/Pd) nanocomposite was synthesised, characterised, and used for cyanide removal from its phenolic mixture. The cyanide-treated effluent was subsequently subjected to biological treatment using the *R. pyridinivorans* strain PDB9T N-1 for the degradation of phenolic compounds. The overall efficiency of this sequential nano-bio process was assessed through several kinetic and thermodynamic models. The mechanism of pollutant removal was thoroughly discussed as well, and the reusability capacity was systematically investigated.

2. Materials and methods

2.1. Chemicals

In this research, all chemicals and reagents used were of analytical reagent grade (AR). Chemicals such as ferric chloride tetrahydrate ($FeCl_3 \cdot 4H_2O$), sodium borohydride ($NaBH_4$), and potassium hexachloropalladate (K_2PdCl_6) were sourced from Merck, India. Polyvinylpyrrolidone (PVP), carboxymethyl cellulose (CMC), and phenol crystals (C_6H_5OH) were sourced from SRL India.

2.2. Methods

2.2.1. Synthesis of nZVI. Nano-zero-valent iron (nZVI) synthesis was carried out according to a modified procedure reported in the literature.[37] In brief, in a three-neck flask, a $NaBH_4$ solution was prepared by adding 4.53 g of $NaBH_4$ to 75 mL of distilled water. Then, the solution was slowly added to 300 mL of a solution containing 4.5 g of $FeCl_3 \cdot 4H_2O$. Meanwhile, N_2 gas was continuously purged to remove oxygen, and the mixture was stirred mechanically. The flow rate was maintained at approximately 0.5 mL per second. Following the addition of $NaBH_4$, the mixture was stirred for an extra 30 minutes to ensure a complete reaction between ferric chloride and sodium borohydride. The Fe^{3+} reduction took place as stated in the following reaction:

$$4Fe^{3+} + 3BH_4^- + 9H_2O \rightarrow 4Fe^0 + 3H_2BO_3- + 12H^+ + 6H_2 \quad (1)$$
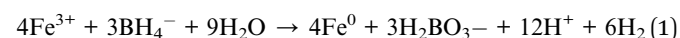
The procedure was carried out until the formation of a black nZVI precipitate. Then, the solution was centrifuged for 10 minutes at 12 000 rpm. The obtained nZVI NMs were washed three times with 100% ethanol, dried at 100 °C, and preserved in an airtight container to prevent further oxidation.

2.2.2. Synthesis of CMC-nZVI. Firstly, the CMC stock solution was prepared by adding 0.2 gm of CMC to 50 mL of a $NaHCO_3$ (1 mM) solution. The CMC stock solution was agitated at 150 rpm using an orbital shaker at 25 °C for 60 min; then, it was placed in the refrigerator overnight to ensure full dissolution and hydration.[25] For the preparation of CMC-coated nZVI, from the stock CMC solution, 37.5 mL was added to 262.5 mL of the $FeCl_3$ solution (15 g L^{-1}). After 30 min, 75 mL of the previously prepared $NaBH_4$ (60.4 g L^{-1}) solution was added to the reaction mixture in a three-neck flask until the black-coloured precipitate formed.

2.2.3. Synthesis of PVP-nZVI. For preparing the PVP-nZVI nanocomposite, first, a PVP solution was prepared by adding 0.25 gm of PVP to 50 mL of distilled water (5 g L^{-1}). From it, 45 mL of PVP was taken and mixed with 255 mL of the $FeCl_3$ solution (15 g L^{-1}). Then, after 30 min, 75 mL of the $NaBH_4$ solution (60.4 g L^{-1}) was added and stirred thoroughly until the formation of a black precipitate. Here, the ratio of PVP was taken as 0.6 g L^{-1} of the total solution.

2.2.4. Synthesis of CMC-PVP-nZVI. In this work, 37.5 mL of the CMC stock solution (0.4 g L^{-1}) and 45 mL of PVP (0.6 g L^{-1}) were added to 217.5 mL of $FeCl_3$ (15 g L^{-1}). The obtained reaction mixture was stirred at 500 rpm for 30 min for complete dissolution; then, 75 mL of $NaBH_4$ (60.4 g L^{-1}) was added and stirred again until the formation of a black precipitate. Then, the precipitate was separated by centrifugation of the solution for 10 minutes at 12 000 rpm. The CMC-PVP-nZVI NPs were washed three times with 100% ethanol, dried at 100 °C and preserved in an airtight container.

2.2.5. Synthesis of CMC-PVP-nZVI/Pd. The synthesis of CMC-PVP-nZVI was done as described above. For palladium doping, the above-synthesized CMC-PVP-nZVI sample was mixed with 10 mL of ethanol, followed by the addition of 10 mg of potassium hexachloropalladate (K_2PdCl_6). Then, the solution was sonicated for 20 min. CMC-PVP/nZVI/Pd was centrifuged at 12 000 rpm for 10 min and dried at 60 °C. The prepared NMs were kept under vacuum overnight and then stored in a sealed container.

2.2.6. Preparation of the *R. pyridinivorans* strain PDB9T N-1 inoculum. The *R. pyridinivorans* strain PDB9T N-1 utilized for this research was first isolated in our laboratory from the local paper pulp wastewater and identified using the 16S rRNA technique.[7,38] The pure culture was grown in an optimized mineral salt medium (MSM) with a phenol concentration ranging from 300 to 2000 mg L^{-1}. MSM was composed of 0.4 g per L KH_2PO_4, 2.64 g per L K_2HPO_4, 0.6 g per L $NaNO_3$, 0.17 g per L $MgSO_4 \cdot 7H_2O$, 0.037 g per L $CaCl_2$, and 0.003 g per L $FeCl_3$.[7] The pH of the culture medium was kept at 7.4. The *R. pyridinivorans* strain PDB9T NS-1 cells were grown in a shaker incubator at 180 rpm and 30 °C. The pure cultures of *R. pyridinivorans* strain PDB9T NS-1 were harvested (with an OD at 600 nm of 1.5) by centrifugation for 10 minutes at 8000 rpm and then used for the phenolic degradation experiments.

2.3. Experimental procedure

2.3.1. Cyanide removal experiment using the synthesised NMs. The cyanide removal experiments using the synthesized NMs were conducted in the batch shake flask operational mode. In this study, cyanide solutions of varying concentrations (20 to 100 mg L^{-1}) were placed in a 100-mL conical flask with 2 g L^{-1} of the NMs for the cyanide removal experiment. The concentration of phenol in the mixed substrate system was fixed at 300 mg L^{-1}. Nitrogen gas was purged for 5 minutes before the addition of NMs to each experimental flask. The pH of the sample was raised to 12.0 using a 1 M NaOH solution in order to prevent cyanide losses due to HCN gas formation. The reaction was performed by constant stirring at 300 rpm, and samples were collected at regular intervals up to 2 h. These collected samples underwent centrifugation at 12 000 rpm, and the supernatant was collected to determine the remaining cyanide concentration using the colorimetric method at 578 nm, as outlined in the literature.[39] The efficiency of cyanide removal was calculated as follows:

$$\text{Removal Efficiency of CN}^-(\%) = \frac{C_0 - C}{C_0} \times 100 \qquad (2)$$

where C_0 is the initial CN^- concentration.

2.3.2. Phenol removal using *R. pyridinivorans* strain PDB9T N-1. Because the CN^- removal experiment was conducted under anaerobic conditions and at a pH of 12, after the removal of cyanide, the treated sample was readjusted to a pH of 7.4 by gradually adding HCl (1 M) and ensuring a sufficient oxygen supply by aerating with an aqua pump. The 48-h cultured *R. pyridinivorans* strain PDB9T N-1 was centrifuged at 8000 rpm, and the biomass was collected. Subsequently, 300 µL of the centrifuged bacterial biomass with an initial $OD_{600\ nm}$ of 1.786 was added to the cyanide-treated experimental conical flask. Then, the experimental flasks were kept in a bacterial incubator shaker at 180 rpm and 30 °C for 24 h. Samples were periodically withdrawn to determine the remaining phenol concentration.

2.4. Analytical method

The cyanide and phenol concentrations were assessed using the PBA method (pyridine-barbituric acid) and 4-amino antipyrine method, respectively, as outlined in standard methods.[38] The developed colours of cyanide and phenol were analysed calorimetrically at 578 nm and 510 nm, respectively, using a UV-Vis spectrophotometer (Evolution 220, Thermo Fisher Scientific, USA). The size distribution, shape, and structure of different synthesized NMs were analyzed by X-ray diffraction (XRD). XRD analysis was conducted using Rigaku Ultima (Japan) by varying the 2θ value between 20° and 90° with X'Pert High Score software. Fourier transform infrared (FTIR) spectroscopy was used to detect the functional groups present on the surface of the NMs using KBr pellets (Thermo Fisher Nicolet 10 spectrometer, USA). FTIR measurements were performed within the 400–4000 cm^{-1} wavenumber range. To examine the structural and morphological configurations of the NMs, the FE-SEM method was utilized (Zeiss Gemini Sigma 300, UK). Using the same Zeiss Gemini Sigma 300 instrument, energy-dispersive X-ray spectroscopy (EDX) was performed to evaluate the compositional purity. X-ray photoelectron spectroscopy (XPS) was used to analyze the surface composition of the nanocomposite using an imaging photoelectron spectrometer (Thermo Escalab, USA), model no. PHI 5000 Versa Probe III.

2.5. Regeneration experiments

After the CN$^-$ removal reaction, the NMs were centrifuged at 12 000 rpm for 10 minutes and dried at 60 $\square$C. Then, the dried NMs were dispersed in a solution of hydrochloric acid (0.1 M). The mixtures were agitated for 120 minutes. To determine the reusability of the NMs, the regeneration experiments of the composites were performed 3 times with HCl; then, the sorbent was cleaned with distilled water till the supernatant had a neutral pH, confirming that there was no acid content on the NMs, which were utilized for the next regeneration cycle.

3. Results and discussion

3.1. Characterization

3.1.1. XRD analysis. X-ray diffraction (XRD) was used to analyze the crystal structure of the synthesized NMs. As shown in Fig. 1(a), the XRD patterns of both nano-zero-valent iron (nZVI) before and after use were analyzed at 2θ values varying from 10° to 80°. The peak seen at 44.76°, related to the 110 plane, shows that iron (Fe) is present, indicating a high level of crystallinity that matches the crystal structures of α-Fe$_2$O$_3$ and γ-Fe$_2$O$_3$, which aligns well with JCPDS file no. 1-1267 for iron.[12,37,40,41] A very small diffraction peak can be observed
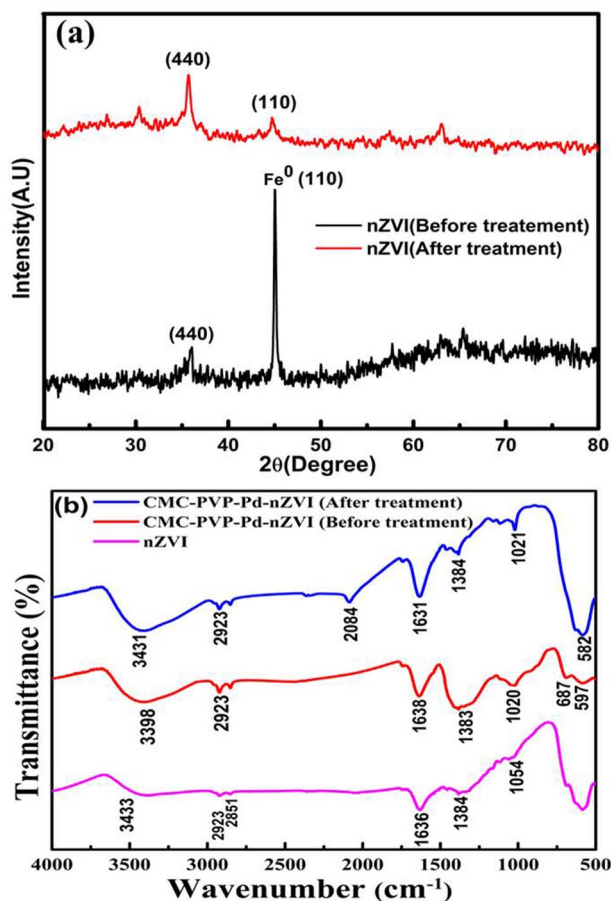

Fig. 1 (a) XRD characterization of nZVI before and after cyanide uptake. (b) FTIR characterization of nZVI and the CMC-PVP-nZVI/Pd nanocomposite before and after cyanide uptake.

around $2\theta \approx 35°$, indicating the presence of a small amount of iron oxides on the particle surface,[29,40] also verified by EDX analysis (26.71%). The presence of this thin amorphous oxide or hydroxide shell surrounding the metallic core (discussed later) supports the characteristic of the core–shell morphology of nZVI, where a reactive Fe^0 core is naturally enclosed by an FeO/Fe$_2$O$_3$/FeOOH surface layer that limits further oxidation while still allowing electron transfer during redox reactions.[42,43] However, the absence of any additional prominent ferric oxide peaks confirms that bulk Fe$_2$O$_3$ formation does not occur. Fig. S1, given in the SI, shows the XRD spectrum of the CMC-PVP-nZVI/Pd nanocomposite. The use of CMC and PVP in the nanocomposite disrupts the normal arrangement of iron atoms, causing X-rays to scatter in different directions. This leads to a significant decrease in the distinct peak of nZVI, indicating the amorphous nature of the CMC-PVP-nZVI/Pd nanocomposite. The XRD patterns of Pd in the CMC-PVP-nZVI/Pd are not detectable, likely due to the low Pd content and the well-dispersed nature of Pd within the CMC-PVP-nZVI/Pd framework. At 34.9°, a small peak is observed, corresponding to the mild oxidation of the outer layer of nZVI.[29,40] These findings align well with the previously reported literature.[40,44] After cyanide uptake, an extra peak is observed in the nZVI sample (Fig. 1(a)) and also in the CMC-PVP-nZVI/Pd composite (Fig. S1), corresponding to iron cyanide [Fe$_4$(Fe(CN)$_6$)$_3$] at a 2θ angle of 35.41°, indexed to the 440 plane,[12] which confirms the reductive sorption of cyanide on the nZVI surface. The FeO peak at 44.8° vanishes after the reaction (Fig. 1(a)), which suggests that the nZVI is completely used for cyanide reduction.[20]

3.1.2. FTIR analysis. Fig. 1(b) displays the FTIR spectrum of nZVI ranging from 4000 to 500 cm^{-1}. The peak at 3433 cm^{-1} is associated with the OH stretching vibration and might be due to H$_2$O, and the peak at 1636 cm^{-1} is partially attributed to the O–H bending vibration of FeOOH.[45] The mild peak at 1067/1054 cm^{-1} suggests the existence of a very small amount of γ-FeOOH lepidocrocite. Fig. 1(b) demonstrates the FTIR spectrum of the CMC-PVP-nZVI/Pd nanocomposite. In the nanocomposite, CMC is effectively attached to the nZVI surface *via* carbonyl (COO–) and hydroxyl (–OH) groups. The presence of COO– and –OH groups results in the formation of longer peaks at 1638 cm^{-1} and near 3398 cm^{-1}, respectively, compared to the fresh nZVI. This observation confirms that CMC molecules have been anchored onto the Fe surface through coordination with hydroxyl and carboxyl groups, as illustrated in Fig. 1(b).[20] The very mild band at 687 cm^{-1} corresponds to the symmetric stretching due to the presence of some Fe–O NMs.[46] After being supported with Pd nanoparticles, the peak at 3433 cm^{-1} is somewhat shifted towards lower wavenumbers, suggesting hydrogen bonding and charge redistribution between the Fe^0/Pd surface and the polymeric coating.[33] Moreover, the peak at 597 cm^{-1} indicates the existence of Pd particles.[47] The increased intensity of the vibration at 1638 cm^{-1}, corresponding to the CO stretching in the CMC-PVP-nZVI/Pd sample, suggests the presence of carbonyl stretching from the pyrrolidone group attached to the nanocomposite. This indicates that PVP has been successfully bonded to Fe through Fe–N interactions.[48,49] After the adsorption process, the FTIR spectra of the nZVI and CMC-

PVP-nZVI/Pd composite were analysed. The presence of the N–H stretching vibration at 3431 cm^{-1} in nZVI after cyanide uptake (Fig. 1(b)) indicates the existence of amine.[12] Another peak is observed in the treated nZVI at 1384 cm^{-1}, which is attributed to the C≡N stretching vibration, suggesting cyanide sorption on the surface of nZVI.[50]

3.1.3. FE-SEM analysis. Fig. 2(a) demonstrates the field-emission scanning electron microscopy (FE-SEM) image of nZVI. From the figure, it can be seen that nZVI is spherical with

an average size of 500 nm (ref. 51) and likely to form chain-like aggregates or multiple spherical particles because of the magnetic attraction between the particles, thereby forming larger, micron-sized particles. Other studies have also observed similar structures of nZVI aggregates.[52,53] Fig. 2(b) illustrates the FE-SEM image of the CMC-PVP-nZVI/Pd nanocomposite. The Fig. 2(b) demonstrates that the nanocomposite (CMC-PVP-nZVI/Pd) is smaller, spherical, and well-dispersed with an average size of 181 nm, whereas nZVI is larger, agglomerated, and irregularly
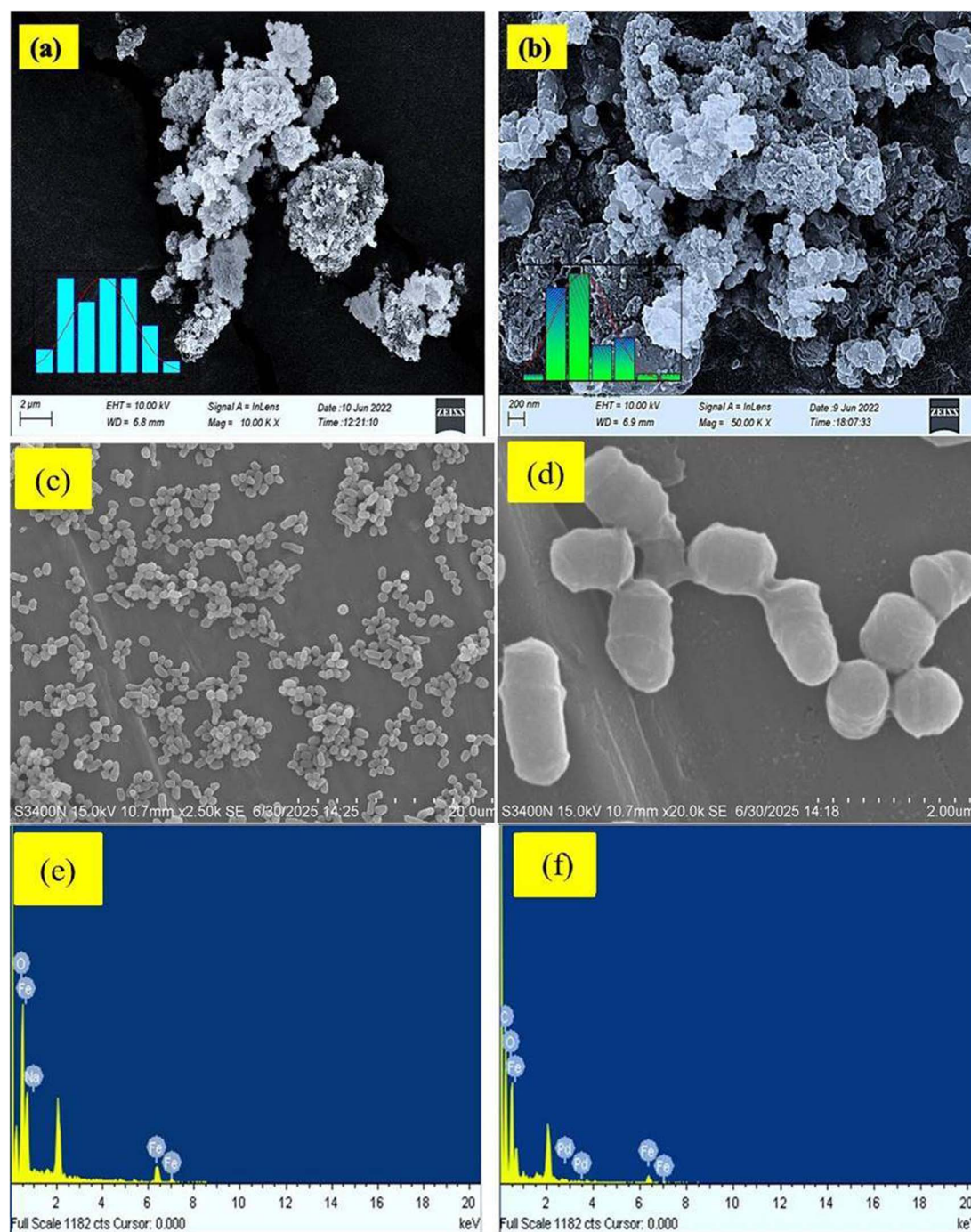

Fig. 2 FE-SEM characterization of the synthesized NMs and *R. pyridinivorans* strain PDB9T N-1: (a) nZVI, (b) CMC-PVP-nZVI/Pd, (c) *R. pyridinivorans* strain PDB9T N-1, and (d) magnified image of *R. pyridinivorans* strain PDB9T N-1. EDX characterization of (e) nZVI and (f) CMC-PVP-nZVI/Pd.

clustered.[54] Furthermore, the composite (CMC-PVP-nZVI/Pd) reveals that the nZVI composites form chain structure-like beads due to the presence of CMC[46] and PVP.[55] Additionally, the size of the nanoparticles decreases gradually due to the addition of CMC.[56] Fig. 2(c) illustrates the FE-SEM image of the *R. pyridinivorans* strain PDB9T N-1. As shown in the figure, the strain PDB9T N-1 does not form a spore and grows as a smooth rod-coccus morphological structure (sometimes irregular). The observation is well matched with *Rhodococcus* sp., as reported in the literature.[57] Fig. 2(d) demonstrates a higher magnification image of the *R. pyridinivorans* strain PDB9T N-1, which reveals a smooth rod-coccus morphological structure.

3.1.4. EDX analysis. The elemental composition of the nanomaterials was analyzed using energy-dispersive X-ray spectroscopy (EDX), as shown in Fig. 2(e and f). The primary elements identified in nZVI were iron (Fe), oxygen (O), and sodium (Na), with weight percentages of 72.40%, 26.71%, and 0.89%, respectively (Fig. 2(e)), indicating the formation of nZVI, which is in good agreement with a previous report in the literature.[12] Here, the presence of a minor Na peak might be due to the use of $NaBH_4$ during synthesis, where residual Na^+ ions remained weakly associated with surface hydroxyl or carboxyl sites even after washing and drying. Furthermore, in the EDX analysis of the CMC-PVP-nZVI/Pd nanocomposite, the main elements detected were iron (Fe), carbon (C), oxygen (O), and palladium (Pd), with weight percentages of 53.36%, 18.63%, 26.61%, and 1.39%, respectively, confirming the existence of palladium and the incorporation of CMC and PVP in the nanocomposite, as illustrated in Fig. 2(f).
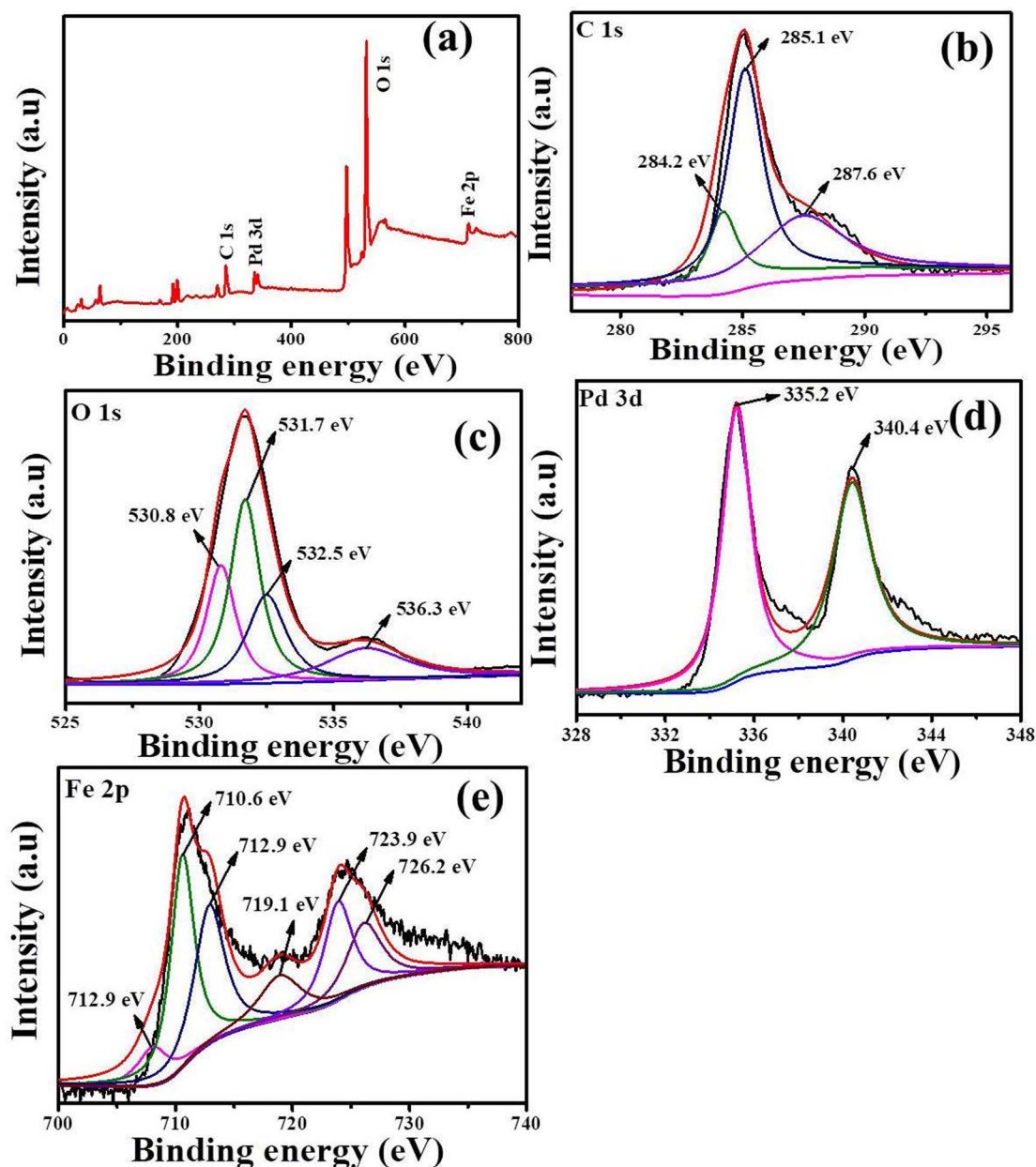

Fig. 3 (a) Full-survey and deconvoluted (b) C 1s, (c) O 1s, (d) Pd, and (e) Fe 2p XPS spectra of the CMC–PVP–nZVI/Pd nanocomposite.

3.1.5. XPS analysis. To further investigate the chemical composition and elemental states of the developed CMC-PVP-nZVI/Pd nanocomposite at the molecular level, XPS analysis was carried out. The results are illustrated in Fig. 3(a–e). Fig. 3(a) shows the survey spectrum of the CMC-PVP-nZVI/Pd nanocomposite, confirming the presence of carbon, oxygen, Pd, and Fe as the major constituent elements. The high-resolution C 1s XPS spectrum of the CMC-PVP-nZVI/Pd nanocomposite can be deconvoluted into three peaks at binding energies of approximately 284.2 eV, 285.1 eV, and 287.6 eV, corresponding to C–C/C–H, C–C–O, and C–C=O/O–C–O bonds, respectively, as shown in Fig. 3(b).[58] These signals generally arise from the hydroxyl, carboxyl, and pyrrolidone groups of CMC and PVP, which

indicate that the polymers are chemically bound to the Fe surface through Fe–O–C and Fe–N linkages. This coordination not only stabilizes the nanoparticles but also facilitates charge delocalization between the Fe and Pd sites, thereby improving electron transfer during redox reactions.[42,59,60] As depicted in Fig. 3(c), the high-resolution O 1s spectra can be fitted with three characteristic peaks located at approximately 530.8 eV, 531.7 eV, and 532.5 eV, corresponding to C=O, C–OH/C–O, and C–OO$^-$/O–C–O functional groups, respectively.[61] The additional shoulder at 536.3 eV can be attributed to adsorbed oxygen from air contaminants and moisture. These oxygenated species confirm the coexistence of polymeric oxygen groups and surface iron oxides or hydroxides, forming a thin passivation layer that protects the
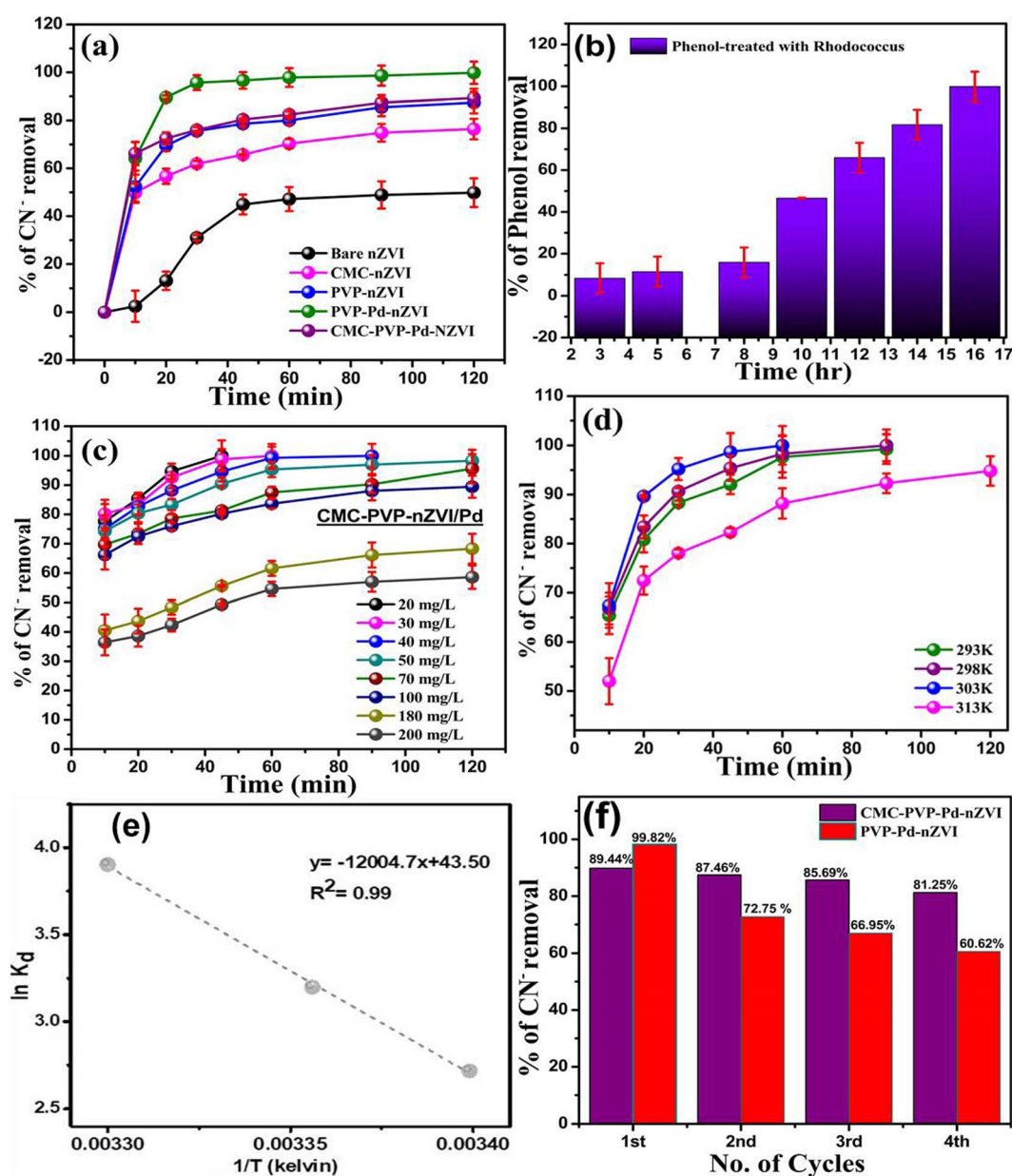
Fig. 4 (a) Efficiency of cyanide removal using individual NMs and the CMC-PVP-nZVI/Pd nanocomposite, (b) biodegradation profile of phenol by *R. pyridinivorans* strain PDB9T N-1, (c) impact of cyanide concentration on its removal by the CMC-PVP-PD-nZVI nanocomposite, (d) effect of temperature on the efficiency of cyanide removal, (e) thermodynamic profile of cyanide removal by the nanocomposite, and (f) regeneration of CMC-PVP-nZVI/Pd and PVP-Pd-nZVI after 3 cycles.*Error bars denote the standard deviation of three independent experimental runs.

Fe^0 core and provides reactive sites for pollutant reduction. As shown in Fig. 3(d), the deconvoluted XPS spectrum of Pd exhibits two distinct peaks at 335.2 eV and 340.4 eV, corresponding to the Pd 3d$_{5/2}$ and Pd 3d$_{3/2}$ orbitals, respectively. These characteristic binding energies confirm that Pd is present in the metallic zero-valent state (Pd^0).[62] Further, a slight negative shift in the Pd binding energy relative to the standard Pd^0 (335.6 eV) suggests electron donation from Fe^0 to Pd, implying a synergistic Fe–Pd coupling that enhances catalytic activity. The Fe 2p profile (Fig. 3(e)) shows two peaks centered at binding energies of 710.6 eV and 723.9 eV, corresponding to Fe(II), while the peaks at 712.9 eV and 726.2 eV are attributed to Fe(III).[63] The presence of Fe(II) and Fe(III) oxides may result from oxidation processes occurring during sample storage or testing. Additionally, the doublet peaks observed at binding energies of 718.9 eV and 707.8 eV correspond to Fe(0) 2p$_{1/2}$ and Fe(0) 2p$_{3/2}$, respectively, confirming that the metallic Fe core remains intact. The simultaneous presence of Fe(0), Fe(II), and Fe(III) signals supports the formation of a core–shell Fe^0/Fe-oxide structure, where the polymer coating and Pd nanoparticles collectively improve structural stability, electron conductivity, and the accessibility of reactive sites within the nanocomposite, demonstrating the effective formation of the CMC-PVP-nZVI/Pd nanocomposite.

3.2. Cyanide removal performance of the synthesized NMs

The cyanide reduction performance of the synthesized NMs is presented in Fig. 4(a). As shown, bare nZVI achieved only 49.65% cyanide removal at an initial dose of 100 mg L^{-1} within 2 h. The incorporation of CMC into nZVI significantly improved the performance, increasing cyanide removal to 76.42%. A further enhancement was observed with PVP-nZVI, which achieved 87.43% removal. The highest efficiency was obtained using the PVP-Pd-nZVI nanocomposite, reaching 99.82% removal. Interestingly, when CMC was introduced into the PVP-Pd-nZVI system (CMC-PVP-nZVI/Pd), the removal efficiency slightly decreased to 89.44%. This reduction can be attributed to the CMC biopolymer coating, which acts as a protective barrier that shields nZVI, thereby slowing its oxidation and deactivation and also partially limiting its reactivity. CMC creates electrostatic and steric forces that push individual nZVI particles apart, thereby maintaining their stability and improving their dispersion in water.[28,29] It also provides the sustained release of nZVI over time, extending its longevity.[53] However, despite these advantages, CMC did not enhance cyanide removal. This reduced efficiency may be attributed to the blocking of nZVI reactive sites by CMC molecules, which serve as stabilizing and coating agents, thus hindering cyanide adsorption and subsequent reduction. In addition, the reductive sorption of cyanide by CMC-PVP-nZVI/Pd was suppressed due to electrostatic repulsion between the negatively charged COO$^-$ groups of CMC and the negatively charged CN$^-$ ions.[20,64] In contrast, PVP significantly improved cyanide reduction by minimizing particle aggregation, increasing the available surface area, and enhancing the electron transfer rate. Further, PVP polymers contain a pyrrole group, which can interact with other molecules, enhancing dispersion and potentially participating in the redox reactions of nZVI.

The incorporation of Pd-doped PVP into nZVI markedly increased cyanide removal efficiency. This improvement is attributed to the ability of Pd^{4+} ions to prevent the further oxidation of iron particles by accepting electrons and being reduced to Pd^{2+}. This process inhibits nZVI oxidation and facilitates the formation of Fe–Pd bimetallic nanoparticles.[34,65] These results demonstrate that PVP-Pd is an effective polymer for enhancing cyanide removal by nZVI. Subsequently, the cyanide-treated sample was subjected to phenol degradation (300 mg L^{-1}) using the *R. pyridinivorans* strain PDB9T, achieving 99.88% phenol removal within 16 h, as shown in Fig. 4(b).

3.3. Phenol degradation performance by *Rhodococcus pyridinivorans* PDB9T N-1

The phenol degradation efficiency of the obtained effluent after nanotreatment was evaluated at an initial phenol concentration of 300 mg L^{-1} over a reaction period of 24 h at pH 7.4. The phenol concentration decreased gradually with time, as shown in Fig. 4(b), reaching 8.32% removal at 2 hours, 46.6% at 10 hours, and 99.88% total degradation by 16 hours. The biological stage was initiated only after complete cyanide removal (<0.1 mg L^{-1}), ensuring that *Rhodococcus pyridinivorans* PDB9T N-1 was not exposed to inhibitory cyanide levels. The consistent increase in the degradation efficiency and the near-complete removal within 16 hours demonstrate the high catalytic activity, adaptability, and robustness of *R. pyridinivorans* in the postdetoxified effluent.

3.4. Effect of the initial cyanide concentration on its removal

The study evaluated the performance of the CMC-PVP-nZVI/Pd nanocomposite at different initial cyanide concentrations ranging from 20 to 200 mg L^{-1} while keeping other parameters constant. Almost complete cyanide removal was observed when the initial concentration was below 40 mg L^{-1}. However, as the cyanide concentration increased, the removal efficiency gradually declined. For example, the efficiency decreased from 100% to 58.6% as the initial dose increased from 40 to 200 mg L^{-1}, as shown in Fig. 4(c). This reduction in efficiency at higher cyanide concentrations can be attributed to the limited availability of active binding sites on the CMC-PVP-nZVI/Pd nanocomposite.[12,66]

3.5. Effect of the temperature and thermodynamics of cyanide removal

Experiments were conducted to examine the effect of the temperature on cyanide removal under fixed conditions (initial cyanide concentration = 100 mg L^{-1}, pH = 12, contact time = 2 h) at four different temperatures (293, 298, 303, and 313 K), as presented in Fig. 4(d). The results indicated that the cyanide removal efficiency increased with rising temperature. This enhancement can be attributed to the disruption of internal bonds within the adsorbent's active sites, which improves the availability of reactive sites for cyanide binding. Moreover, the higher temperature lowers the solution's viscosity, thereby facilitating cyanide sorption onto nZVI.[12,63] Remarkably, almost complete removal (>99%) was achieved at 303 K. The impact of

the temperature on the sorption dynamics of cyanide can be analysed using thermodynamic principles, where $\Delta G°$, $\Delta H°$, and $\Delta S°$ denote the Gibbs free energy, enthalpy, and entropy, respectively. The values of these thermodynamic parameters were computed using the following equations:

$$\Delta G° = - RT \ln k_d \qquad (3)$$

$$k_d = \frac{q_e}{c_e} \qquad (4)$$

In this context, k_d represents the adsorption equilibrium constant, T represents the temperature in Kelvin, and R is the universal gas constant (8.314 J mol^{-1} K^{-1}).

$$\Delta G° = \Delta H° - T\Delta S° \qquad (5)$$

The van't Hoff equation is obtained by combining eqn (4) and (5), as shown below:

$$\ln k_d = \frac{\Delta S°}{R} - \frac{\Delta H°}{RT} \qquad (6)$$

The slope of the thermodynamic plot of $1/T$ *vs.* $\ln k_d$ yielded a positive enthalpy change ($\Delta H°$) of 99.80 kJ mol^{-1}. Fig. 4(e) reveals that the cyanide removal process is endothermic. However, when the temperature was raised to 313 K (Fig. 4(d)), more water molecules desorbed, and the increased molecular energy weakened the attractive forces between them, which subsequently decreased the sorption rate.[67] The Gibbs free energy changes ($\Delta G°$) at different temperatures were determined to be -105.86, -107.67, and -109.78 kJ mol^{-1}, as presented in Table 1. The negative $\Delta G°$ value indicates that cyanide removal is a spontaneous process, with chemisorption likely being the dominant mechanism. The positive entropy change ($\Delta S°$) suggests an increased degree of disorder at the solid–liquid interface, which may result from structural reorganization as cyanide ions bind to the active sites of the nanocomposite.

3.6. Regeneration and recycling of the nanocomposite

Reducing the production cost of adsorption materials is crucial, and regeneration methods play an important role in this regard. Acid washing is a widely used technique to restore NMs by removing their passivation layer.[68] After four regeneration cycles, the CMC-PVP-nZVI/Pd nanocomposite maintained a high cyanide removal efficiency of 81.25% (Fig. 4(f)), likely due to the protective CMC coating on nZVI. This demonstrates that CMC-PVP-nZVI/Pd is a cost-effective material for treating cyanide-contaminated water. In contrast, the regeneration

efficiency of PVP-nZVI/Pd was only 60.6%, lower than that of the complete CMC-PVP-nZVI/Pd composite, confirming that the CMC coating enhances the stability and longevity of nZVI.

Although the PVP-nZVI/Pd composite exhibited the highest cyanide removal efficiency (99.82%), its catalytic activity rapidly declined upon reuse due to aggregation and oxidation. The addition of CMC led to a slight decrease in performance (89.44%). This decline is mainly due to the partial coverage of reactive Fe^0 sites by CMC molecules, which act as stabilizing agents and restrict the direct contact between Fe^0 and cyanide ions. Moreover, the negatively charged carboxyl (–COO$^-$) groups of CMC may repel cyanide anions (CN$^-$), further limiting adsorption and reduction. Despite this reduction in the initial efficiency, the incorporation of CMC provided substantial benefits in terms of stability and recyclability. The CMC coating prevented oxidation, minimized particle aggregation, and maintained catalytic activity over several reuse cycles. Hence, a clear balance emerged. While PVP-nZVI/Pd was more efficient in a single treatment, the CMC-PVP-nZVI/ Pd composite offered greater durability and operational reliability, making it more suitable for long-term and cost-effective wastewater treatment.

3.7. Kinetics of cyanide removal using the CMC-PVP-nZVI/ Pd nanocomposite

3.7.1. Pseudo-first and second-order kinetic models. The analysis of reductive sorption kinetics is crucial for understanding both the rate and controlling mechanisms of the reductive sorption process, including mass transfer and physicochemical reactions.[69,70] The pseudo-first-order kinetic model effectively describes the rate of physisorption, highlighting the dependence of the process on the availability of unoccupied sites on the adsorbent surface.[38,71] This model is based on the Lagergren equation and is expressed as follows:

$$\ln (q_e - q_t) = \ln q_e - K_1 t \qquad (7)$$

In eqn (7), q_t is the reductive adsorption capacity at a given time t and q_e is the equilibrium adsorption capacity. Here, the constant K_1 is the rate of adsorption. In contrast, the kinetics of chemisorption can be explained using the pseudo-second-order model. The simplified representation of the pseudo-second-order model can be expressed as follows:

$$\frac{t}{q_t} = \frac{1}{K_2 q_e^2} + \frac{t}{q_e} \qquad (8)$$

where K_2 is the adsorption rate constant. Fig. 5 shows the kinetics of cyanide removal using the CMC-PVP-nZVI/Pd nanocomposite. The pseudo-second-order model fits well with the experimental data, which shows a very high R^2 value of 0.99 compared to the pseudo-first-order model, as shown in Fig. 5(a and b). The larger R^2 value of the pseudo-second-order model indicates that chemisorption plays a major role and is dominant over the physical adsorption process for cyanide removal. In the solution, the free sites on the adsorbent surface share or exchange electrons with the cyanide ions in the chemisorption process,[69,71] thereby aiding in the removal of cyanide. The

Table 1 Thermodynamic parameter values for the degradation of cyanide using CMC-PVP-nZVI/Pd

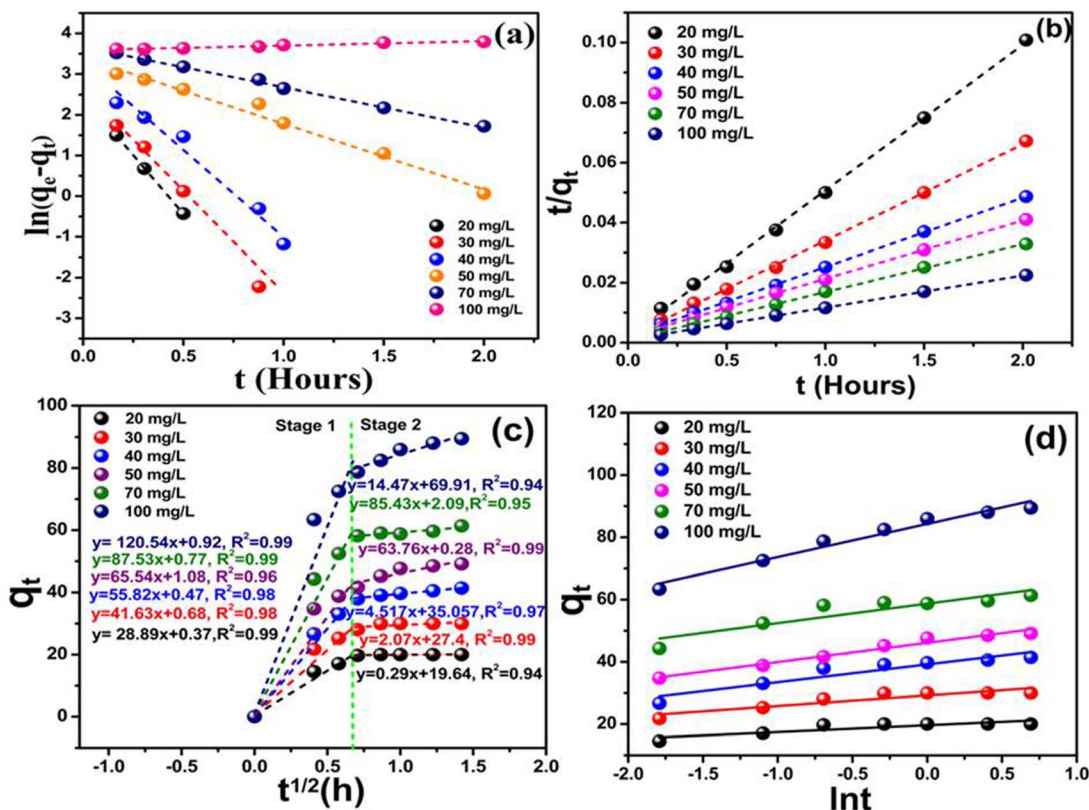| Temperature (K)	K_d	$\Delta G°$ (kJ mol^{-1})	$\Delta H°$ (kJ mol^{-1})	$\Delta S°$ (J mol^{-1} K^{-1})
293	15.125	-105.86	99.8	361.659
298	24.5	-107.67		
303	49.5	-109.78		

Fig. 5 Analysis of cyanide reductive sorption kinetics utilizing the CMC–PVP–nZVI/Pd nanocomposite: (a) pseudo-first-order model, (b) pseudo-second-order model, (c) intraparticle diffusion, and (d) Elovich model.

theoretical cyanide reductive sorption capacity calculated using the pseudo-second-order model is 93.37 mg g^{-1}, closely matching the experimentally observed value of 89.44 mg g^{-1}.

3.7.2. Intraparticle diffusion model. The intraparticle diffusion model provides a deeper understanding of the mass transfer mechanism in porous adsorbents, describing the interactions between the adsorbent and adsorbate during the reductive sorption process.[38] The intraparticle diffusion behaviour of an adsorbent is described by the Morris and Webber model, and its linear representation is shown as follows:

$$q_t = K_3 t^{1/2} + C_1 \qquad (9)$$

where the constant K_3 represents the rate of intraparticle diffusion. According to this model, if the plot of q_t *vs.* $t^{1/2}$ is linear, it indicates that the intraparticle diffusion process is the primary mechanism controlling reductive sorption. In the case of multilinear curves in the data set, the whole process is governed by more than one stage. In the present study, the appearance of a multilinear regression pattern indicates that cyanide removal involves two stages, as illustrated in Fig. 5(c). The initial stage represents the external mass transfer of cyanide from the solution phase to the solid–liquid interface of the CMC–PVP–nZVI/Pd nanocomposite. The second stage involves the diffusion of cyanide into the internal pores of the CMC–PVP–nZVI/Pd nanocomposite. A steeper slope and a higher correlation coefficient in the first stage indicate a faster adsorption process, suggesting that the cyanide removal rate is largely governed by external mass

transfer. In the second stage, the lower slope shows that the intraparticle diffusion process is very slow and insignificant for the removal of cyanide, as shown in Fig. 5(c). A similar observation is also well explained in the literature.[38,70] Additionally, the K_{3i} value for cyanide removal is greater than K_{3ii}, demonstrating that external mass transfer is the rate-limiting step, with minimal intraparticle diffusion.[72] This is in line with other reports,[69,72] wherein a lower K_2 value than K_1 has been reported.

3.7.3. Elovich model. The Elovich model is primarily influenced by highly active heterogeneous surface functional groups, which are closely associated with the chemisorption process. According to this model, the adsorption rate decreases exponentially as the amount of the adsorbate increases.[73] The Elovich model also indicates that both the diffusion process and the reaction rate play significant roles in controlling the reductive sorption. The equation used in the model is as follows:

$$q_t = \frac{1}{\beta} \ln(\alpha\beta) + \frac{1}{\beta} \ln t \qquad (10)$$

where the initial adsorption velocity is denoted by α (mg g^{-1} h^{-1}) and the chemisorption surface coverage parameter and activation energy are denoted by β (g mg^{-1}).[69] In this study, α and β are used to represent the initial rate constant of surface coverage and chemisorption activation energy, respectively. Fig. 5(d) presents the q_t *vs.* ln t graph. The slope of the line represents $\frac{1}{\beta}$, and the intercept corresponds to $\frac{1}{\beta} \ln (\alpha\beta)$; the calculated β value is 0.0939, as presented in Table 1. The lower β value observed in this

study suggests that the chemisorption process has high feasibility. Similarly, the α value of the adsorption rate is calculated to be 29 319.26 mg g^{-1} h^{-1} with an R^2 of 0.96. This suggests that the reductive sorption of cyanide on the CMC-PVP-nZVI/Pd nanocomposite is primarily driven by chemisorption rather than physisorption, which is further confirmed by the rapid cyanide reductive sorption process.[74] Hence, it can be concluded that cyanide removal on the CMC-PVP-nZVI/Pd nanocomposite probably occurs according to surface exchange reactions until the available sites on the surface are saturated.

3.8 Stabilization mechanisms

To prevent the aggregation of nZVI particles and enhance their catalytic activity and conductivity, various stabilization strategies have been developed, with carboxymethyl cellulose (CMC) being one of the most effective. The stabilization process involves several critical stages. The overall mechanism of sequential cyanide and phenolic removal by the CMC-PVP-nZVI/Pd nanocomposite and *R. pyridinivorans* strain PDB9T is illustrated in Fig. 6. In the initial stage, CMC, a water-soluble polymer derived from cellulose, adsorbs onto the nZVI surface, forming a protective coating. This coating acts as a physical and electrostatic barrier, preventing particle aggregation and shielding nZVI from the rapid oxidation and deactivation caused by direct exposure to the surrounding environment. The incorporation of CMC also helps reduce the dissolution rate of nZVI. By forming a protective coating, CMC not only enhances the reduction capacity of nZVI but also enables the sustained release of reducing agents over an extended period, thereby improving the longevity of nZVI.[75] Similarly, PVP is employed as a conductive polymer due to its superior charge storage capacity and low scattering loss[49]. The PVP coating significantly enhances the stability and reactivity of nZVI particles, resulting in improved pollutant removal efficiency.[76] Furthermore, the unique structure of PVP, characterized by rigid pyrrole groups, promotes the formation of complexes with various inorganic compounds, underscoring its suitability for polymeric nanomaterial synthesis, as illustrated in Fig. 6.[77] In this study, PVP is employed as both a highly conductive material and a stabiliser to synthesise stable and efficient nZVI. The introduced Pd^{4+} ions prevent further oxidation of iron particles by accepting electrons and reducing to Pd^{2+}, thereby protecting nZVI from oxidation and facilitating the formation of Fe–Pd bimetallic nanoparticles.[29] Palladium not only enhances the reactivity of nZVI but also inhibits atmospheric oxidation on its surface.[18,41]

The overall mechanism of cyanide removal by the CMC-PVP-nZVI/Pd nanocomposite involves Pd-assisted reductive chemisorption. Initially, the XRD peak at 35.41° (440 plane) indicates that CN$^-$ ions are chemisorbed onto Fe^0 active sites, forming transient Fe–CN surface complexes (Fe$_4$[Fe(CN)$_6$]$_3$).[12]

$$Fe^0 + CN^- \rightarrow Fe - CN$$
$$\text{(surface complexation/chemisorption)} \quad (11)$$
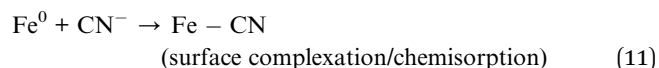
The FTIR spectra further support this mechanism. After cyanide uptake, nZVI exhibits an N–H stretching band at
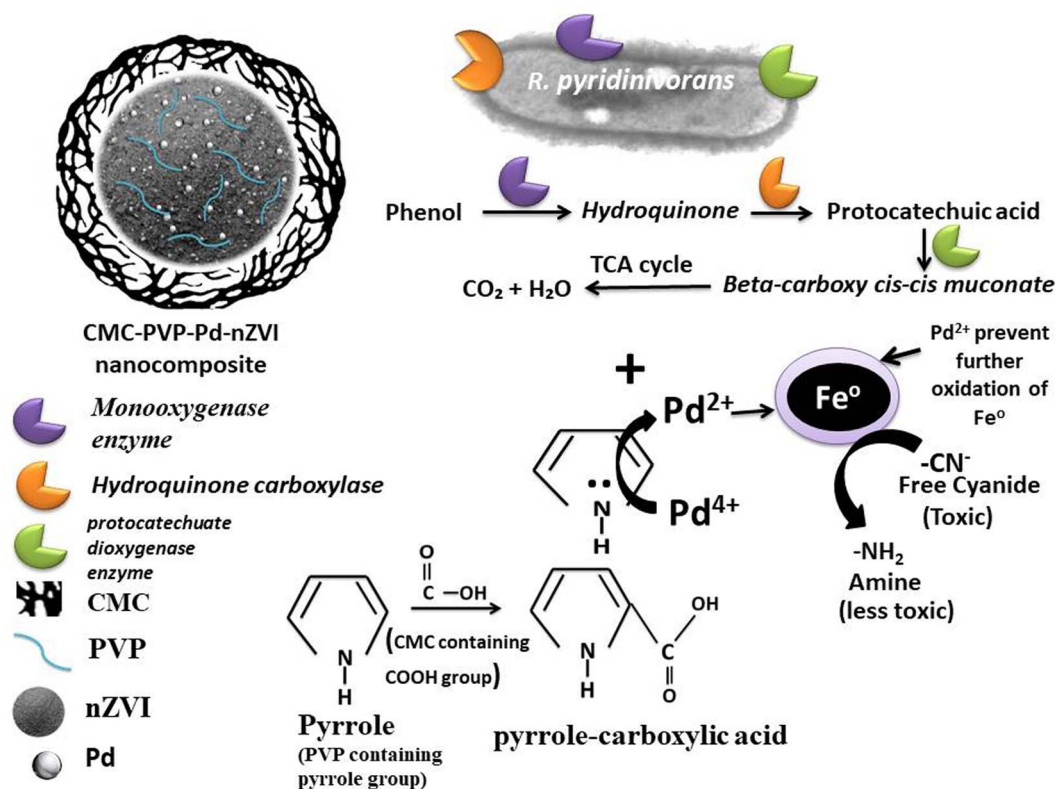

Fig. 6 Detailed mechanism of sequential cyanide and phenol removal by the CMC-PVP-nZVI/Pd nanocomposite and *R. pyridinivorans* strain PDB9T.

3431 cm^{-1}, confirming the formation of amine groups,[12] and a distinct C≡N stretching band at 1384 cm^{-1}, confirming cyanide sorption and partial reduction.[50] The N–H signal reveals that CN$^-$ undergoes reductive transformation to less-toxic amine species, facilitated by Pd catalysis. During synthesis, K$_2$PdCl$_6$ (Pd^{4+}) serves as the palladium precursor and is spontaneously reduced by Fe^0 through a two-step reduction process:[78–80]

$$Fe^0 + Pd^{4+} \rightarrow Fe^{2+} + Pd^{2+} \tag{12}$$

$$Fe^0 + Pd^{2+} \rightarrow Fe^{2+} + Pd^0 \tag{13}$$
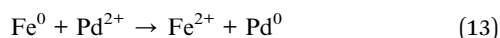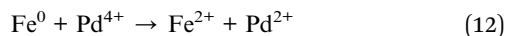
This reduction leads to the deposition of bimetallic Pd^0 nanoparticles on the Fe^0 surface, forming a bimetallic Fe–Pd^0 structure.[81] This is well agreement with the XPS analysis, wherein the deconvoluted XPS spectrum of Pd exhibits two distinct peaks at 335.2 eV and 340.4 eV, corresponding to the Pd 3d$_{5/2}$ and Pd 3d$_{3/2}$ orbitals, respectively. These characteristic binding energies confirm that Pd is present in the metallic zero-valent state (Pd^0).[62]

Consequently, the CMC-PVP-nZVI/Pd nanocomposite exhibits the highest cyanide removal of 99% at an initial dose of 100 mg L^{-1}. Following cyanide removal, the filtered sample is subsequently utilized for the next phase of phenol degradation. The degradation of phenol is caused by the phenol mono-oxygenase enzyme of *Rhodococcus pyridinivorans* N-1, which converts phenol into hydroquinone. The hydroquinone is then subjected to an oxidation reaction to generate protocatechuic acid by hydroquinone carboxylase. Later, the protocatechuate is converted to beta-carboxy *cis–cis* muconate by a ring-fission reaction catalysed by the protocatechuate dioxygenase enzyme system. This is followed by several decarboxylation and oxidation reactions to generate TCA cycle intermediates, ultimately leading to complete mineralization into CO$_2$ and H$_2$O.[7] This enzymatic sequence transforms phenol into less-toxic intermediates and finally into harmless end products.

4. Conclusion

In this study, the synthesized nanomaterials (NMs) were characterized and evaluated for cyanide removal. The FTIR and XPS analyses confirmed that the functional groups, such as hydroxyl, carbonyl, and pyrrolidone groups, of CMC and PVP chemically interacted with the Fe/Pd surface through Fe–O–C and Fe–N linkages. This coordination improved electron delocalization between Fe^0 and Pd, increased the accessibility of active sites, and enhanced the overall redox reactivity of the nanocomposite. The coating of polymers also provided both steric and electrostatic stabilization that successfully inhibited nZVI aggregation, as confirmed by FE-SEM analysis. The stabilized CMC-PVP-nZVI/Pd nanocomposite achieved more than 99% cyanide removal at an initial concentration of 100 mg L^{-1} at 30 °C, demonstrating 1.8-fold higher efficiency than bare nZVI. Kinetic studies revealed that cyanide removal by CMC-PVP-nZVI/Pd followed a pseudo-second-order model, indicating a chemisorption mechanism with a high sorption capacity of 93.37 mg g^{-1}. While PVP-nZVI/Pd exhibited the maximum cyanide removal efficiency, the CMC-PVP-nZVI/Pd nanocomposite showed superior regeneration performance, highlighting the role of CMC in enhancing the stability and longevity of nZVI. This balance between the initial efficiency and durability underscores its practical value, providing a sustainable and reusable solution for continuous industrial wastewater treatment. Thermodynamic analysis further confirmed the spontaneity of the sorption process (negative $\Delta G°$) and its endothermic nature (positive $\Delta H°$). In parallel, the isolated strain *Rhodococcus pyridinivorans* PDB9T demonstrated effective phenol removal from partially treated wastewater. Together, this sequential nano-bio treatment system presents a promising, economical, and environmentally sustainable strategy for treating hazardous industrial effluents.

Author contributions

Ankita Priyadarshini: conduct experiments, investigation, methodology, formal analysis, validation, data curation, writing – original draft. Naresh Kumar Sahoo: investigation, conceptualization, supervision, analyzed sample and data, writing draft manuscript, writing – review and editing, funding acquisition, project administration, funding resources. Soumya Mishra: conduct experiments, investigation, methodology, formal analysis, validation, data curation, and writing – original draft. Prasanta Kumar Sahoo: conceptualization, analyzed sample and data, writing draft manuscript, formal analysis, review & editing. Ranjan Kumar Bhuyan: conceptualization, supervision, visualization, data curation, formal analysis, review, and editing. Prangya Ranjan Rout: conceptualization, supervision, visualization, data curation, formal analysis, review, and editing. Bankim Chandra Tripathy: conceptualization, supervision, visualization, data curation, formal analysis, review, and editing.

Conflicts of interest

There are no conflicts to declare.

Data availability

Data will be made available on request.

Supplementary information (SI) is available. See DOI: https://doi.org/10.1039/d5na00920k.

Acknowledgements

References

1 N. K. Sharma and L. Philip, Combined biological and photocatalytic treatment of real coke oven wastewater, *Chem. Eng. J.*, 2016, **295**, 20–28.

2 X. Xiang, M. Zhang, Q. Huang, Y. Mao, J. Jia, X. Zeng, Y. Dong, J. Liao, X. Chen and X. Yao, *et al*, Construction of S-scheme $CuInS_2/ZnIn_2S_4$ heterostructures for enhanced photocatalytic activity towards Cr (VI) removal and antibiotics degradation, *Chemosphere*, 2024, **352**, 141351.

3 N. Panigrahy, M. Barik and N. K. Sahoo, Kinetics of phenol biodegradation by an indigenous Pseudomonas citronellolis NS1 isolated from coke oven wastewater, *J. Hazard., Toxic Radioact. Waste*, 2020, **24**, 4020019.

4 J. Mishra, D. S. Pattanayak, A. A. Das, D. K. Mishra, D. Rath and N. K. Sahoo, Enhanced photocatalytic degradation of cyanide employing Fe-porphyrin sensitizer with hydroxyapatite palladium doped TiO_2 nano-composite system, *J. Mol. Liq.*, 2019, **287**, 110821.

5 D. S. Pattanayak, J. Mishra, J. Nanda, P. K. Sahoo, R. Kumar and N. K. Sahoo, Photocatalytic degradation of cyanide using polyurethane foam immobilized Fe-TCPP-S-TiO_2-rGO nano-composite, *J. Environ. Manage.*, 2021, **297**, 113312.

6 S. Bhattacharya, A. A. Das, G. C. Dhal, P. K. Sahoo, A. Tripathi and N. K. Sahoo, Evaluation of N doped rGO-ZnO-CoPc $(COOH)_8$ nanocomposite in cyanide degradation and its bactericidal activities, *J. Environ. Manage.*, 2022, **302**, 114022.

7 M. Barik, C. P. Das, A. K. Verma, S. Sahoo and N. K. Sahoo, Metabolic profiling of phenol biodegradation by an indigenous Rhodococcus pyridinivorans strain PDB9T N-1 isolated from paper pulp wastewater, *Int. Biodeterior. Biodegrad.*, 2021, **158**, 105168.

8 A. K. Bakthavatsalam, *et al*, A comparative study on growth and degradation behavior of C. pyrenoidosa on synthetic phenol and phenolic wastewater of a coal gasification plant, *J. Environ. Chem. Eng.*, 2019, **7**, 103079.

9 S. K. Sahoo, A. A. Das, D. Deka, B. Naik and N. K. Sahoo, Organic-inorganic hybrid hydroquinone bridged V-CdS/HAP/Pd-TCPP: A novel visible light active photocatalyst for phenol degradation, *J. Mol. Liq.*, 2021, **339**, 116721.

10 T. Felföldi, Z. Nagymáté, A. J. Székely, L. Jurecska and K. Márialigeti, Biological treatment of coke plant effluents: from a microbiological perspective, *Biol. Futura*, 2020, **71**, 359–370.

11 S. C. Curry and M. B. Spyres, Cyanide: hydrogen cyanide, inorganic cyanide salts, and nitriles, in *Critical Care Toxicology*, Springer, 2015, pp. 1–21.

12 M. Tyagi, A. Rana, S. Kumari and S. Jagadevan, Adsorptive removal of cyanide from coke oven wastewater onto zero-valent iron: Optimization through response surface methodology, isotherm and kinetic studies, *J. Clean. Prod.*, 2018, **178**, 398–407.

13 A. Alvillo-Rivera, S. Garrido-Hoyos, G. Buitrón, P. Thangarasu-Sarasvathi and G. Rosano-Ortega, Biological treatment for the degradation of cyanide: A review, *J. Mater. Res. Technol.*, 2021, **12**, 1418–1433.

14 U. Singh, N. K. Arora and P. Sachan, Simultaneous biodegradation of phenol and cyanide present in coke-oven effluent using immobilized Pseudomonas putida and Pseudomonas stutzeri, *Braz. J. Microbiol.*, 2018, **49**, 38–44.

15 J. Chen, H. Luo, D. Luo, Y. Chen, J. Tang, H. Ma and S. Pu, New insights into the degradation of nitrobenzene by activated persulfate with sulfidated nanoscale zero-valent iron: Synergistic effects of reduction and reactive oxygen species oxidation, *Sep. Purif. Technol.*, 2023, **322**, 124252.

16 Y. Zou, X. Wang, A. Khan, P. Wang, Y. Liu, A. Alsaedi, T. Hayat and X. Wang, Environmental remediation and application of nanoscale zero-valent iron and its composites for the removal of heavy metal ions: a review, *Environ. Sci. Technol.*, 2016, **50**, 7290–7304.

17 D. O'Carroll, B. Sleep, M. Krol, H. Boparai and C. Kocur, Nanoscale zero valent iron and bimetallic particles for contaminated site remediation, *Adv. Water Resour.*, 2013, **51**, 104–122.

18 Y. Gao, F. Wang, Y. Wu, R. Naidu and Z. Chen, Comparison of degradation mechanisms of microcystin-LR using nanoscale zero-valent iron (nZVI) and bimetallic Fe/Ni and Fe/Pd nanoparticles, *Chem. Eng. J.*, 2016, **285**, 459–466.

19 M. Fu, Q. Jiao and Y. Zhao, One-step vapor diffusion synthesis of uniform CdS quantum dots/reduced graphene oxide composites as efficient visible-light photocatalysts, *RSC Adv.*, 2014, **4**, 23242–23250.

20 R. Eljamal, O. Eljamal, I. Maamoun, G. Yilmaz and Y. Sugihara, Enhancing the characteristics and reactivity of nZVI: Polymers effect and mechanisms, *J. Mol. Liq.*, 2020, **315**, 113714.

21 J. Shi, J. Wang, W. Wang, W. Teng and W. Zhang, Stabilization of nanoscale zero-valent iron in water with mesoporous carbon (nZVI@ MC), *J. Environ. Sci.*, 2019, **81**, 28–33.

22 J. Deng, H. Dong, C. Zhang, Z. Jiang, Y. Cheng, K. Hou, L. Zhang and C. Fan, Nanoscale zero-valent iron/biochar composite as an activator for Fenton-like removal of sulfamethazine, *Sep. Purif. Technol.*, 2018, **202**, 130–137.

23 C. Wang, H. Luo, Z. Zhang, Y. Wu, J. Zhang and S. Chen, Removal of As (III) and As (V) from aqueous solutions using nanoscale zero valent iron-reduced graphite oxide modified composites, *J. Hazard. Mater.*, 2014, **268**, 124–131.

24 E. Lefevre, N. Bossa, M. R. Wiesner and C. K. Gunsch, A review of the environmental implications of in situ remediation by nanoscale zero valent iron (nZVI): behavior, transport and impacts on microbial communities, *Sci. Total Environ.*, 2016, **565**, 889–901.

25 H. Dong, F. Zhao, G. Zeng, L. Tang, C. Fan, L. Zhang, Y. Zeng, Q. He, Y. Xie and Y. Wu, Aging study on carboxymethyl cellulose-coated zero-valent iron nanoparticles in water: Chemical transformation and structural evolution, *J. Hazard. Mater.*, 2016, **312**, 234–242.

26 T. Phenrat, N. Saleh, K. Sirk, H.-J. Kim, R. D. Tilton and G. V Lowry, Stabilization of aqueous nanoscale zerovalent iron dispersions by anionic polyelectrolytes: adsorbed anionic polyelectrolyte layer properties and their effect on aggregation and sedimentation, *J. Nanoparticle Res.*, 2008, **10**, 795–814.

27 T. Phenrat, N. Saleh, K. Sirk, R. D. Tilton and G. V Lowry, Aggregation and sedimentation of aqueous nanoscale zerovalent iron dispersions, *Environ. Sci. Technol.*, 2007, **41**, 284–290.

28 Y. Xie, Y. Yi, Y. Qin, L. Wang, G. Liu, Y. Wu, Z. Diao, T. Zhou and M. Xu, Perchlorate degradation in aqueous solution using chitosan-stabilized zero-valent iron nanoparticles, *Sep. Purif. Technol.*, 2016, **171**, 164–173.

29 F. He and D. Zhao, Manipulating the size and dispersibility of zerovalent iron nanoparticles by use of carboxymethyl cellulose stabilizers, *Environ. Sci. Technol.*, 2007, **41**, 6216–6221.

30 H. Wang, C. Jin, X. Li, J.-X. Ma, Y.-F. Ye, L.-X. Tang, J. Si and B.-K. Cui, A green biocatalyst fabricated by fungal laccase immobilized onto Fe$_3$O$_4$@ polyaniline-chitosan nanofibrous composites for the removal of phenolic compounds, *Chem. Eng. J.*, 2025, **507**, 160486.

31 J. Y. Lu, Z. Q. Bu, Y. Q. Lei, D. Wang, B. He, J. Wang and W. T. Huang, Facile microwave-assisted synthesis of Sb$_2$O$_3$-CuO nanocomposites for catalytic degradation of p-nitrophenol, *J. Mol. Liq.*, 2024, **409**, 125503.

32 Y. Li, J. Bu, Y. Sun, Z. Huang, X. Zhu, S. Li, P. Chen, Y. Tang, G. He and S. Zhong, Efficient degradation of norfloxacin by synergistic activation of PMS with a three-dimensional electrocatalytic system based on Cu-MOF, *Sep. Purif. Technol.*, 2025, **356**, 129945.

33 J. Xie, C. Lei, W. Chen and B. Huang, Conductive-polymer-supported palladium-iron bimetallic nanocatalyst for simultaneous 4-chlorophenol and Cr (VI) removal: Enhanced interfacial electron transfer and mechanism, *J. Hazard. Mater.*, 2022, **424**, 127748.

34 F. He, D. Zhao, J. Liu and C. B. Roberts, Stabilization of Fe-Pd nanoparticles with sodium carboxymethyl cellulose for enhanced transport and dechlorination of trichloroethylene in soil and groundwater, *Ind. Eng. Chem. Res.*, 2007, **46**, 29–34.

35 Z.-B. Wang, J. Zhang, Q. Miao, H.-Y. Cao, F. Xiong, T. Lee, A. El-Baz, L. Xie and S.-Q. Ni, Achieving stable partial denitrification by selective inhibition of nitrite reductase with the biosafe aprotic solvent DMSO, *Environ. Sci. Technol.*, 2024, **58**, 21242–21250.

36 Z. Qi, S. Wen, Z. Liu and D. Jiang, Oxygen-promoted 6-endo-trig cyclization of β, γ-unsaturated hydrazones/ketoximes with diazonium tetrafluoroborates for pyridazin-4 (1 H)-ones/oxazin-4 (1 H)-ones, *Org. Lett.*, 2023, **25**, 6110–6115.

37 W. Shen, X. Wang, F. Jia, Z. Tong, H. Sun, X. Wang, F. Song, Z. Ai, L. Zhang and B. Chai, Amorphization enables highly efficient anaerobic thiamphenicol reduction by zero-valent iron, *Appl. Catal., B*, 2020, **264**, 118550.

38 A. Priyadarshini, S. Mishra, N. K. Sahoo, S. Raut, A. Daverey and B. C. Tripathy, Biodegradation of phenol using the indigenous Rhodococcus pyridinivorans Strain PDB9T NS-1 immobilized in calcium alginate beads, *Appl. Biochem. Biotechnol.*, 2024, **196**, 2798–2818.

39 S. Mishra, N. K. Sahoo, P. K. Sahoo, S. Sahoo, L. Nayak and P. R. Rout, Construction of a novel ternary synergistic CuFe$_2$O$_4$-SnO$_2$-rGO heterojunction for efficient removal of cyanide from contaminated water, *RSC Adv.*, 2024, **14**, 13850–13861.

40 S. Mandal, S. Pu, L. Shangguan, S. Liu, H. Ma, S. Adhikari and D. Hou, Synergistic construction of green tea biochar supported nZVI for immobilization of lead in soil: A mechanistic investigation, *Environ. Int.*, 2020, **135**, 105374.

41 C. H. Nguyen, M. L. Tran, T. T. Van Tran and R.-S. Juang, Efficient removal of antibiotic oxytetracycline from water by Fenton-like reactions using reduced graphene oxide-supported bimetallic Pd/nZVI nanocomposites, *J. Taiwan Inst. Chem. Eng.*, 2021, **119**, 80–89.

42 C. He, Y. Ding, C. Li, W. Yan, A. Mao, S. Wei and M. Li, Cost-effective core@ shell structured zero-valent iron nanoparticles@ magnetic (nZVI@ Fe$_3$O$_4$) for Cr (VI) removal from aqueous solutions: preparation by disproportionation of Fe (ii), *RSC Adv.*, 2023, **13**, 26983–26994.

43 M. Liu, Y. Ye, L. Xu, T. Gao, A. Zhong and Z. Song, Recent advances in nanoscale zero-valent iron (nZVI)-based advanced oxidation processes (AOPs): Applications, mechanisms, and future prospects, *Nanomaterials*, 2023, **13**, 2830.

44 F. Jiao, J.-C. Jumas, M. Womes, A. V Chadwick, A. Harrison and P. G. Bruce, Synthesis of ordered mesoporous Fe$_3$O$_4$ and γ-Fe$_2$O$_3$ with crystalline walls using post-template reduction/oxidation, *J. Am. Chem. Soc.*, 2006, **128**, 12905–12909.

45 R. Singh, V. Misra and R. P. Singh, Synthesis, characterization and role of zero-valent iron nanoparticle in removal of hexavalent chromium from chromium-spiked soil, *J. Nanoparticle Res.*, 2011, **13**, 4063–4073.

46 L. Qian, S. Liu, W. Zhang, Y. Chen, D. Ouyang, L. Han, J. Yan and M. Chen, Enhanced reduction and adsorption of hexavalent chromium by palladium and silicon rich biochar supported nanoscale zero-valent iron, *J. Colloid Interface Sci.*, 2019, **533**, 428–436.

47 M. Sarmah, A. B. Neog, P. K. Boruah, M. R. Das, P. Bharali and U. Bora, Effect of substrates on catalytic activity of biogenic palladium nanoparticles in C–C cross-coupling reactions, *ACS Omega*, 2019, **4**, 3329–3340.

48 I. A. Safo, M. Werheid, C. Dosche and M. Oezaslan, The role of polyvinylpyrrolidone (PVP) as a capping and structure-directing agent in the formation of Pt nanocubes, *Nanoscale Adv.*, 2019, **1**, 3095–3106.

49 L. Chen, T. Yuan, R. Ni, Q. Yue and B. Gao, Multivariate optimization of ciprofloxacin removal by polyvinylpyrrolidone stabilized NZVI/Cu bimetallic particles, *Chem. Eng. J.*, 2019, **365**, 183–192.

50 H. Uppal, S. S. Tripathy, S. Chawla, B. Sharma, M. K. Dalai, S. P. Singh, S. Singh and N. Singh, Study of cyanide removal from contaminated water using zinc peroxide nanomaterial, *J. Environ. Sci.*, 2017, **55**, 76–85.

51 H. Khorsandi, A. Azarnioush, A.-A. Aghapour, S. Nemati, S. Karimzadeh and H.-R. Khalkhali, An analysis of boron removal from water using modified zero-valent iron nanoparticles, *Desalin. Water Treat.*, 2017, **70**, 284–289.

52 Y.-H. Shih, C.-P. Tso and L.-Y. Tung, Rapid degradation of methyl orange with nanoscale zerovalent iron particles, *Nanotechnology*, 2010, **7**, 7.

53 H. K. Boparai, M. Joseph and D. M. O'Carroll, Cadmium (Cd^{2+}) removal by nano zerovalent iron: surface analysis, effects of solution chemistry and surface complexation modeling, *Environ. Sci. Pollut. Res.*, 2013, **20**, 6210–6221.

54 A. Saberinasr, M. Rezaei, M. Nakhaei and S. M. Hosseini, Transport of CMC-stabilized nZVI in saturated sand column: The effect of particle concentration and soil grain size, *Water Air Soil Pollut.*, 2016, **227**, 1–16.

55 D. Edikresnha, I. Sriyanti, M. M. Munir, *et.al*, in *IOP Conference Series: Materials Science and Engineering*, 2017, vol. 202, p. 12043.

56 H. Zhou, M. Ma, Y. Zhao, S. A. Baig, S. Hu, M. Ye and J. Wang, Integrated green complexing agent and biochar modified nano zero-valent iron for hexavalent chromium removal: A characterisation and performance study, *Sci. Total Environ.*, 2022, **834**, 155080.

57 W. Guo, J. Duan, Z. Shi, X. Yu and Z. Shao, Biodegradation of PET by the membrane-anchored PET esterase from the marine bacterium Rhodococcus pyridinivorans P23, *Commun. Biol.*, 2023, **6**, 1090.

58 J.-L. Zhu, M.-L. Wang, S.-C. Shi, J.-X. Ren, H.-D. Huang, W. Lin and Z.-M. Li, In-situ constructing robust cellulose nanocomposite hydrogel network with well-dispersed dual catalysts for the efficient, stable and recyclable photo-Fenton degradation, *Cellulose*, 2022, **29**, 1929–1942.

59 R. Shamshirgaran, R. Malakooti, A. Akbarpour and A. Z. Moghaddam, Fabrication of Polyvinylpyrrolidone-Stabilized Nano Zero-Valent Iron Supported by Hydrophilic Biochar for Efficient Cr (VI) Removal from Groundwater, *ChemistrySelect*, 2022, **7**, e202202927.

60 B. Zhang, J. Zhan, J. Fan, B. Zhu, W. Shen, S. Zhang, W. Li, Z. Li and F. Zeng, Application of Carboxymethyl Cellulose (CMC)-Coated Nanoscale Zero-Valent Iron in Chromium-Containing Soil Remediation, *Clean Technol.*, 2024, **6**, 1610–1624.

61 Y. O. Al-Ghamdi, M. Jabli, M. H. Alhalafi, A. Khan and K. A. Alamry, Hybridized sulfated-carboxymethyl cellulose/MWNT nanocomposite as highly selective electrochemical probe for trace detection of arsenic in real environmental samples, *RSC Adv.*, 2023, **13**, 18382–18395.

62 Z. Zhu, S. Liang, H. Sun, W. Zhang, J. Yang and Z. Gao, Magnetic Pd–Fe nanoparticles for sustainable Suzuki–Miyaura cross-coupling reactions, *Catal. Sci. Technol.*, 2024, **14**, 3176–3183.

63 A. Jena, B. Mahanty, D. Deka, P. K. Sahoo, S. Pradhan, P. R. Rout, S. Mishra and N. K. Sahoo, Green synthesis of a potential magnetic and mesoporous EG-nZVI/CA-MCM41 nanocomposite for reductive sorption of europium, *Environ. Sci. Nano*, 2024, **11**, 855–869.

64 L. Gong, S. Shi, N. Lv, W. Xu, Z. Ye, B. Gao, D. M. O'carroll and F. He, Sulfidation enhances stability and mobility of carboxymethyl cellulose stabilized nanoscale zero-valent iron in saturated porous media, *Sci. Total Environ.*, 2020, **718**, 137427.

65 G.-H. Han, S.-H. Lee, M. Seo and K.-Y. Lee, Effect of polyvinylpyrrolidone (PVP) on palladium catalysts for direct synthesis of hydrogen peroxide from hydrogen and oxygen, *RSC Adv.*, 2020, **10**, 19952–19960.

66 B. Agarwal, C. Balomajumder and P. K. Thakur, Simultaneous co-adsorptive removal of phenol and cyanide from binary solution using granular activated carbon, *Chem. Eng. J.*, 2013, **228**, 655–664.

67 J. E. Asuquo, I. S. Udegbunam and E. E. Etim, Effect of temperature on the adsorption of metallic soaps of castor seed oil onto haematite, *Int. J. Adv. Res. Chem. Sci*, 2017, **4**, 345–353.

68 J. Yang, L. Zhou, F. Ma, H. Zhao, F. Deng, S. Pi, A. Tang and A. Li, Magnetic nanocomposite microbial extracellular polymeric substances@ Fe_3O_4 supported nZVI for Sb (V) reduction and adsorption under aerobic and anaerobic conditions, *Environ. Res.*, 2020, **189**, 109950.

69 A. Jena, N. K. Sahoo, P. K. Sahoo, S. Mishra, P. R. Rout and Y. Zhong, Design of a novel green synthesized ZVS/S-rGO-Deinococcus radiodurans R1 chitosan hydrogel beads for enhanced recovery of europium, *J. Clean. Prod.*, 2025, 145367.

70 F. Liu, W. Huang, S. Wang and B. Hu, Investigation of adsorption properties and mechanism of uranium (VI) and europium (III) on magnetic amidoxime-functionalized MCM-41, *Appl. Surf. Sci.*, 2022, **594**, 153376.

71 N. Singh and C. Balomajumder, Phytoremediation potential of water hyacinth (Eichhornia crassipes) for phenol and cyanide elimination from synthetic/simulated wastewater, *Appl. Water Sci.*, 2021, **11**, 144.

72 Y. Huang, X. Lee, M. Grattieri, F. C. Macazo, R. Cai and S. D. Minteer, A sustainable adsorbent for phosphate removal: modifying multi-walled carbon nanotubes with chitosan, *J. Mater. Sci.*, 2018, **53**, 12641–12649.

73 K. Riahi, S. Chaabane and B. Ben Thayer, A kinetic modeling study of phosphate adsorption onto Phoenix dactylifera L. date palm fibers in batch mode, *J. Saudi Chem. Soc.*, 2017, **21**, S143–S152.

74 P. Zong, M. Shao, D. Cao, X. Xu, S. Wang and H. Zhang, Synthesis of potential Ca–Mg–Al layered double hydroxides coated graphene oxide composites for simultaneous uptake of europium and fulvic acid from wastewater systems, *Environ. Res.*, 2021, **196**, 110375.

75 X. Kong, L. Xuan, Y. Fu, F. Yuan and C. Qin, Effect of the modification sequence on the reactivity, electron selectivity, and mobility of sulfidated and CMC-stabilized nanoscale zerovalent iron, *Sci. Total Environ.*, 2021, **793**, 148487.

76 J. Li, M. Fan, M. Li and X. Liu, Cr (VI) removal from groundwater using double surfactant-modified nanoscale zero-valent iron (nZVI): Effects of materials in different status, *Sci. Total Environ.*, 2020, **717**, 137112.

77 S. Bubel, N. Mechau and R. Schmechel, Electronic properties of polyvinylpyrrolidone at the zinc oxide nanoparticle surface: PVP in ZnO dispersions and nanoparticulate ZnO thin films for thin film transistors, *J. Mater. Sci.*, 2011, **46**, 7776–7783.

78 S. Park, J. E. Zenobio and L. S. Lee, Perfluorooctane sulfonate (PFOS) removal with Pd0/nFe0 nanoparticles: adsorption or

aqueous Fe-complexation, not transformation?, *J. Hazard. Mater.*, 2018, **342**, 20–28.

79 H.-L. Lien and W. Zhang, Nanoscale iron particles for complete reduction of chlorinated ethenes, *Colloids Surf., A*, 2001, **191**, 97–105.

80 C. Noubactep, On the operating mode of bimetallic systems for environmental remediation, *J. Hazard. Mater.*, 2009, **164**, 394–395.

81 X. Wang, C. Chen, Y. Chang and H. Liu, Dechlorination of chlorinated methanes by Pd/Fe bimetallic nanoparticles, *J. Hazard. Mater.*, 2009, **161**, 815–823.